ELectronics EXpress

LETTER

IEICE Electronics Express, Vol.15, No.14, 1–11

Resonant transmission through periodic subwavelength real metal slits in the terahertz range

Sungjun Yoo[1], **Jong-Eon Park**[2a)], **and Hosung Choo**[1]

[1] *School of Electronic and Electrical Engineering, Hongik University, 94, Wausan-ro, Mapo-gu, Seoul, Korea*

[2] *Metamaterial Electronic Device Research Center, Hongik University, 94, Wausan-ro, Mapo-gu, Seoul, Korea*

a) *jongeon.park@gmail.com*

Abstract: This article investigates the resonant transmission characteristics of periodic subwavelength slits on real metallic plates at terahertz frequencies. By applying the eigenvalues of the slit to the mode matching technique (MMT), the transmission characteristics of the periodic subwavelength slits can be resolved as function of the gap width, plate thickness, and frequency. The resulting transmittance of the proposed method is then verified by comparing it with a commercial electromagnetic simulation software. This study demonstrates that the proposed MMT is suitable for calculating the transmittance of the periodic metal-insulator-metal slits on the real metal material and provides in-depth intuition for resonance phenomena using the modal approach.

Keywords: metal-insulator-metal waveguide, mode matching, transmittance, subwavelength slit

Classification: Electromagnetic theory

References

[1] R. F. Harrington and D. T. Auckland: "Electromagnetic transmission through narrow slots in thick conducting screens," IEEE Trans. Antennas Propag. **28** (1980) 616 (DOI: 10.1109/TAP.1980.1142382).

[2] J. Bravo-Abad, *et al.*: "Transmission properties of a single metallic slit: From the subwavelength regime to the geometrical-optics limit," Phys. Rev. E **69** (2004) 026601 (DOI: 10.1103/PhysRevE.69.026601).

[3] F. J. García-Vidal, *et al.*: "Light passing through subwavelength apertures," Rev. Mod. Phys. **82** (2010) 729 (DOI: 10.1103/RevModPhys.82.729).

[4] B. Sturman, *et al.*: "Eigenmodes for metal-dielectric light-transmitting nanostructures," Phys. Rev. B **76** (2007) 125104 (DOI: 10.1103/PhysRevB.76.125104).

[5] B. Sturman, *et al.*: "Theory of extraordinary light transmission through arrays of subwavelength slits," Phys. Rev. B **77** (2008) 075106 (DOI: 10.1103/PhysRevB.77.075106).

[6] Ş. E. Kocabaş, *et al.*: "Modal analysis and coupling in metal-insulator-metal waveguides," Phys. Rev. B **79** (2009) 035120 (DOI: 10.1103/PhysRevB.79.

DOI: 10.1587/elex.15.20180612
Received June 12, 2018
Accepted June 19, 2018
Publicized July 2, 2018
Copyedited July 25, 2018

035120).
[7] B. Sturman, *et al.*: "Optical properties of periodic arrays of subwavelength slits in a perfect metal," Phys. Rev. B **84** (2011) 205439 (DOI: 10.1103/PhysRevB.84.205439).
[8] J.-E. Park, *et al.*: "Analysis of deep-subwavelength Au and Ag slit transmittances at terahertz frequencies," J. Opt. Soc. Am. B **33** (2016) 1355 (DOI: 10.1364/JOSAB.33.001355).
[9] F. L. Teixeira: "Time-domain finite-difference and finite-element methods for Maxwell equations in complex media," IEEE Trans. Antennas Propag. **56** (2008) 2150 (DOI: 10.1109/TAP.2008.926767).
[10] A. D. Rakić, *et al.*: "Optical properties of metallic films for vertical-cavity optoelectronic devices," Appl. Opt. **37** (1998) 5271 (DOI: 10.1364/AO.37.005271).
[11] N. Zhang and W. Nah: "Mode analysis of cascaded four-conductor lines using extended mixed-mode S-parameters," J. Electromagn. Eng. Sci. **16** (2016) 57 (DOI: 10.5515/JKIEES.2016.16.1.57).
[12] J. Won, *et al.*: "Identifying the appropriate position on the ground plane for MIMO antennas using characteristic mode analysis," J. Electromagn. Eng. Sci. **16** (2016) 119 (DOI: 10.5515/JKIEES.2016.16.2.119).
[13] W. C. Chew: *Waves and Fields in Inhomogeneous Media* (Wiley, New York, 1999).
[14] A. Wexler: "Solution of waveguide discontinuities by modal analysis," IEEE Trans. Microw. Theory Techn. **15** (1967) 508 (DOI: 10.1109/TMTT.1967.1126521).
[15] Remcom: XFdtd 3D electromagnetic simulation software (2018) https://www.remcom.com.

1 Introduction

Resonant power transmission through a one-dimensional (1-D) single or periodic slit is a classical research topic [1, 2, 3]. In previous studies, the electromagnetic transmission and reflection phenomena at the interface between free space and a metallic slit are calculated by assuming a metal to be a perfect electric conductor (PEC). However, since the metal is no longer PEC at higher terahertz (THz) frequencies, the material properties of real metal should be taken into account to obtain the accurate transmission and reflection in a metal-insulator-metal (MIM) waveguide [4, 5, 6]. Thus, there has been efforts to solve the real metal transmittances by several approaches, such as modal analyses for a 1-D single MIM slit [4, 5] and periodic MIM slits [6, 7]. However, the studies were limited because the material properties of metals were chosen arbitrarily or only specific THz frequencies were considered. Although the resonant transmission phenomena through a metallic slit have been investigated at wide THz frequencies [8], the study only provided the transmission characteristics of a single MIM slit case, which means a non-periodic structure.

The subwavelength slit transmittance problems can be analyzed by various numerical methods [8, 9], such as finite-difference time-domain (FDTD) method, finite element method, method of moments, etc. However, the brute-force techniques give us to know physics a posteriori, but mode matching technique (MMT)

DOI: 10.1587/elex.15.20180612
Received June 12, 2018
Accepted June 19, 2018
Publicized July 2, 2018
Copyedited July 25, 2018

provides more direct insight in the physics for the problem [6, 8] by obtaining the distribution of eigenvalues and corresponding modal profiles with respect to the parameters of the slit geometry.

In this paper, we examine the resonant transmission through a periodic MIM slit by considering the material properties of real metals at wide THz frequencies. The transmission and reflection coefficients at two interfaces are obtained, one is from free space to the periodic MIM slit and the other is in the reverse direction. In order to achieve the transmission and reflection coefficients, eigenvalues in the periodic MIM slit should be solved and applied to MMT. By using all modal coefficients, the reflection and transmission characteristics for the three-layer structure are accurately obtained as a function of the THz frequency, gap width, and thickness of the MIM plate. We then compare the results of the PEC and discuss the delicate differences between the transmission characteristics of the two real metals. The resulting transmittance of the proposed method is also verified by comparing it with a commercial electromagnetic (EM) simulation software. Finally, the magnetic field distributions at resonance and off-resonance are investigated for the real metal slits to make it easier to understand and compare the resonance phenomena.

2 Geometry and dispersion equation

Fig. 1 shows the geometry to be analyzed and can be divided into three regions. Regions 1 and 3 are free space, and the periodic MIM slit in Region 2 is resided between the two regions. The periodic MIM slit consists of the metal, insulator, and metal, where the dimensions of the metal and insulator are $2h_m$ and $2h_v$, respectively. The period p of the MIM slit is $2(h_m + h_v)$, and the thickness of the MIM plate is w. The insulator used in the Region 2 is vacuum, and the plate is a real metal. The entire geometry is invariant along the y-axis. The interfaces between the free space (Regions 1 and 3) and the periodic MIM slit (Region 2) are represented as Junctions 1 and 2, respectively. It is assumed that the TM wave (parallel polarization) is incident along the z-axis since the resonant transmission phenomena are more clearly observed than the case of TE wave (perpendicular polarization) incidence. The transmittance is defined as the ratio of the transmitted power to the incident power.

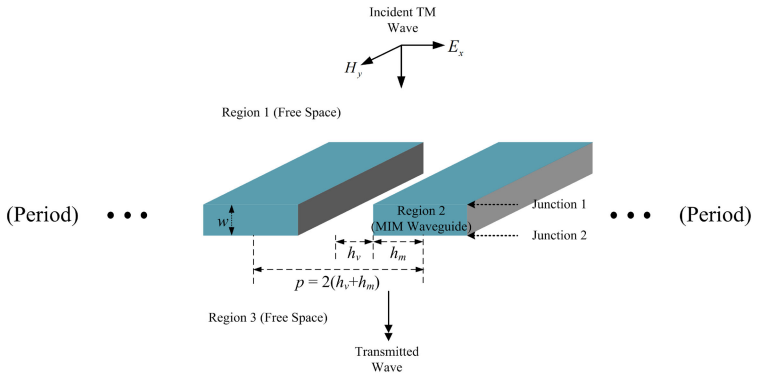

Fig. 1. Geometry of the periodic MIM slit.

DOI: 10.1587/elex.15.20180612
Received June 12, 2018
Accepted June 19, 2018
Publicized July 2, 2018
Copyedited July 25, 2018

The transmission properties are then examined in accordance with the width $2h_v$ of vacuum, the thickness w of the plate, and the material properties of metals that are variables according to the frequencies as listed in Table I [10]. To obtain the transmission characteristics through the subwavelength periodic MIM slit by MMT, the modes in the MIM waveguide should be analyzed and can be obtained from the dispersion equation [6, 8, 11, 12] as follows:

$$\frac{\kappa_{v,n}}{\varepsilon_v}\tanh(\kappa_{v,n}h_v)+\frac{\kappa_{m,n}}{\varepsilon_m}\tanh(\kappa_{m,n}h_m)=0 \tag{1}$$

$$k_{z,n}^2=\kappa_{m,n}^2+\omega^2\mu\varepsilon_m=\kappa_{v,n}^2+\omega^2\mu\varepsilon_v \tag{2}$$

ε_m and ε_v are permittivities in metal and vacuum, respectively. $\kappa_{m,n}$ and $\kappa_{v,n}$ are the n^{th} transverse propagation constants in metal and vacuum, respectively, and $k_{z,n}$ is the n^{th} propagation constant along z-axis. The subscripts n in $\kappa_{m,n}$, $\kappa_{v,n}$, and $k_{z,n}$ commonly indicate the n^{th} modes. Once the roots of the dispersion Eq. (1) $\kappa_{m,n}$ are solved by Muller's method, then the $\kappa_{v,n}$, and $k_{z,n}$ can be easily found by Eq. (2).

Table I. Relative permittivities of Al and Ag

Frequency (THz)	Silver	Aluminum
30	$-3738.3-j\ 1487.3$	$-6361.9-j\ 3670.2$
50	$-1470.8-j\ 355.65$	$-2776.2-j\ 1294.0$
200	$-94.108-j\ 7.567$	$-213.96-j\ 42.987$

Fig. 2 presents the roots of normalized propagation constant (NPC) k_z/k_0 in the point spectrum and the discretized continuous spectrum (DCS) of the periodic MIM waveguide. Al is used as metal with $p=0.8\lambda_0$ and $2h_v=0.2\lambda_0$ at 200 THz. Note that $\mathrm{Im}(k_z/k_0)\le 0$ since the positive $\mathrm{Im}(k_z/k_0)$ amplifies the wave as each mode advances. The point spectrum in red squares indicates the sinusoidal harmonics of H_y-field patterns mainly in the insulator of the periodic MIM waveguide.

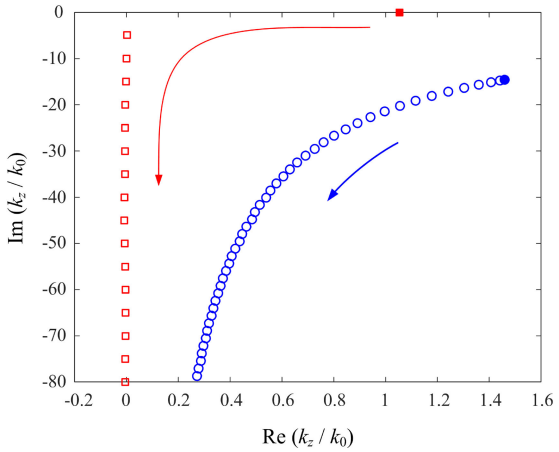

Fig. 2. Point and discretized continuous spectra in the proposed MIM slit.

As can be seen in Fig. 2, the imaginary part of the point spectrum decreases gradually as the modal order increases, similar to the trend of eigenvalues of the

DOI: 10.1587/elex.15.20180612
Received June 12, 2018
Accepted June 19, 2018
Publicized July 2, 2018
Copyedited July 25, 2018

parallel plate waveguide (PPW). The propagation effect by the first mode of the point spectrum is dominant since the imaginary parts of all other modes except for the first mode are very large, resulting in drastic attenuation. The $\mathrm{Re}(k_z/k_0)$ and $\mathrm{Im}(k_z/k_0)$ of the first mode in the point spectrum are 1.053 and -0.005, respectively, which contributes to the propagation with little attenuation. The DCS in blue circles indicates that the sinusoidal harmonics of H_y-field patterns mainly placed in the metal of the periodic MIM waveguide. All values of $\mathrm{Im}(k_z/k_0)$ are less than -10 and have little effect on propagation, contributing only to satisfaction of the boundary conditions when applying MMT [6, 8]. The magnetic fields of both spectra in the periodic MIM slit can be expressed as:

$$H_{y,n}(x) = \begin{cases} \cosh(\kappa_{v,n}x)/\cosh(\kappa_{v,n}h_v), & 0 \le x \le h_v \\ \cosh(\kappa_{m,n}(x - h_v - h_m))/\cosh(\kappa_{m,n}h_m), & h_v \le x \le (h_v + h_m) \end{cases} \tag{3}$$

3 Mode matching technique

To solve the transmittance in Fig. 1, the MMT is applied, and the reflection and transmission coefficients for each Junction described in Fig. 3 are obtained. After combining the coefficients, the total transmittance from Region 1 to Region 3 is calculated accurately by taking into account the multi-layer problems [13]. Figs. 3(a) and 3(b) show the geometries by emphasizing the Junctions 1 and 2. The electromagnetic fields at Junction 1 in Fig. 3(a) can be expressed as follows:

$$a_k^{Inc}\vec{E}_{Fk}^{Inc} + \sum_{i=1}^{N_F} a_i^{Rfl}\vec{E}_{Fi}^{Rfl} = \sum_{j=1}^{N_M} b_j^{Trans}\vec{E}_{Mj}^{Trans} \tag{4a}$$

$$a_k^{Inc}\vec{H}_{Fk}^{Inc} - \sum_{i=1}^{N_F} a_i^{Rfl}\vec{H}_{Fi}^{Rfl} = \sum_{j=1}^{N_M} b_j^{Trans}\vec{H}_{Mj}^{Trans} \tag{4b}$$

where the $\vec{E}_{Fk}^{Inc}$ and $\vec{H}_{Fk}^{Inc}$ present the k-th modal incident electric and magnetic fields in Region 1, and the $\vec{E}_{Fi}^{Rfl}$ and $\vec{H}_{Fi}^{Rfl}$ show the i-th modal reflected electric and magnetic fields in Region 1, respectively. The $\vec{E}_{Mj}^{Trans}$ and $\vec{H}_{Mj}^{Trans}$ indicate the j-th modal transmitted electric and magnetic fields in Region 2. N_F and N_M are the total number of modes used in Regions 1 and 2. The subscript F and M represent the free space and the MIM waveguide. An incident coefficient a_k^{Inc}, reflected coefficients a_i^{Rfl}, and transmitted coefficients b_j^{Trans} are described in Eqs. (4a) and (4b). Here a_k^{Inc} is a given coefficient, and the $\{a_i^{Rfl}\}$s and the $\{b_j^{Trans}\}$s are the coefficients to be solved. By weighting the $\vec{H}_{Fi}^{Rfl}$ in Eq. (4a) and $\vec{E}_{Mj}^{Trans}$ in Eq. (4b), N_F and N_M equations can be obtained, respectively. This expansion of equations and a solving procedure are introduced in detail in [14]. Then, the reflection and transmission coefficients at Junction 1 are completely solved.

Similarly, the incident, reflected, and transmitted electromagnetic fields in Regions 2 and 3 around Junction 2 in Fig. 3(b) are expressed as:

DOI: 10.1587/elex.15.20180612
Received June 12, 2018
Accepted June 19, 2018
Publicized July 2, 2018
Copyedited July 25, 2018

$$
\begin{aligned}
c_1^{Inc}\vec{E}_{M1}^{Inc} + \sum_{j=1}^{N_M} c_j^{Rfl}\vec{E}_{Mj}^{Rfl} &= \sum_{i=1}^{N_F} d_i^{Trans}\vec{E}_{Fi}^{Trans} \\
c_2^{Inc}\vec{E}_{Mk}^{Inc} + \sum_{j=1}^{N_M} c_j^{Rfl}\vec{E}_{Mj}^{Rfl} &= \sum_{i=1}^{N_F} d_i^{Trans}\vec{E}_{Fi}^{Trans} \\
&\vdots \\
c_{N_M}^{Inc}\vec{E}_{M(N_M)}^{Inc} + \sum_{j=1}^{N_M} c_j^{Rfl}\vec{E}_{Mj}^{Rfl} &= \sum_{i=1}^{N_F} d_i^{Trans}\vec{E}_{Fi}^{Trans}
\end{aligned}
\tag{5a}
$$

$$
\begin{aligned}
c_1^{Inc}\vec{H}_{M1}^{Inc} - \sum_{j=1}^{N_M} c_j^{Rfl}\vec{H}_{Mj}^{Rfl} &= \sum_{i=1}^{N_F} d_i^{Trans}\vec{H}_{Fi}^{Trans} \\
c_2^{Inc}\vec{H}_{M2}^{Inc} - \sum_{j=1}^{N_M} c_j^{Rfl}\vec{H}_{Mj}^{Rfl} &= \sum_{i=1}^{N_F} d_i^{Trans}\vec{H}_{Fi}^{Trans} \\
&\vdots \\
c_{N_M}^{Inc}\vec{H}_{M(N_M)}^{Inc} - \sum_{j=1}^{N_M} c_j^{Rfl}\vec{H}_{Mj}^{Rfl} &= \sum_{i=1}^{N_F} d_i^{Trans}\vec{H}_{Fi}^{Trans}
\end{aligned}
\tag{5b}
$$

where the incident coefficients $c_1^{Inc}, c_2^{Inc}, \cdots, c_{N_M}^{Inc}$ are given, and the reflected and transmitted coefficients of $\{c_j^{Rfl}\}$s and $\{d_i^{Trans}\}$s are the coefficients to be calculated. In the same way in Eqs. (4), the coefficients can be solved for Junction 2.

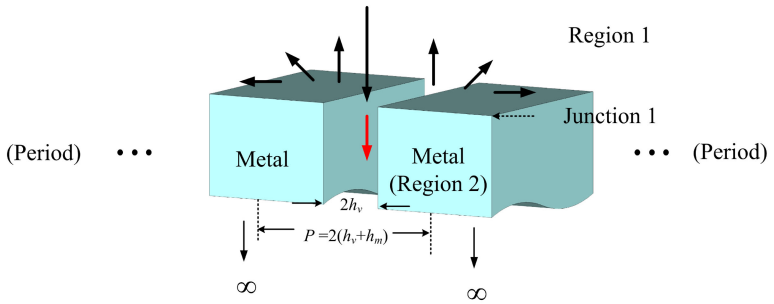

(a) Junction 1

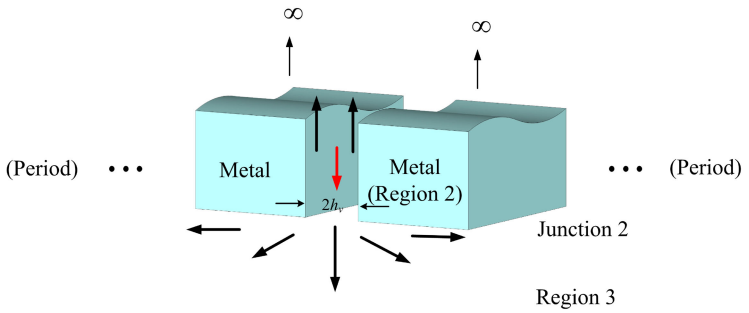

(b) Junction 2

Fig. 3. Geometry of the MIM waveguide at Junctions 1 and 2.

DOI: 10.1587/elex.15.20180612
Received June 12, 2018
Accepted June 19, 2018
Publicized July 2, 2018
Copyedited July 25, 2018

Table II. TM_0 mode reflection and transmission coefficients for PEC, Al, and Ag at Junction 1, when $2h_v = 0.2\lambda_0$ and $2(h_m + h_v) = 0.8\lambda_0$

Metal	Reflection coefficients	Transmission coefficients
PEC	0.6967∠166.83°	1.4346∠26.28°
Al at 200 THz	0.6273∠161.92°	1.4117∠23.12°
Ag at 200 THz	0.5839∠164.09°	1.3667∠21.96°

When the Eqs. (4) are solved, the reflection and transmission coefficients for Al, Ag, and PEC at 200 THz are obtained at Junction 1 and are listed in Table II. The incident power density is assumed to be 1 W/m^2, and the dimensions for the width $2h_v$ and the period $p = 2(h_m + h_v)$ are $0.2\lambda_0$ and $0.8\lambda_0$. The amplitudes of the TM_0 reflection and transmission coefficients for the PEC are obtained as 0.6967 and 1.4346. The coefficients for the real metals are slightly smaller than those of PEC because the waves penetrate the real metals and consequently dissipate as ohmic loss. The amplitudes of both coefficients for Ag are smaller than those of Al, due to the unique relative permittivities mentioned in Table I.

Figs. 4(a) and 4(b) show the amplitudes of the first eleven TM modal transmission coefficients for Figs. 3(a) and 3(b) in the case of Al. The dimensions $2h_v$ and p in the x-axis are $0.2\lambda_0$ and $0.8\lambda_0$. When the TM_0 mode is excited from Region 1, the reflected and transmitted modes can be calculated at Junction 1, and the transmission coefficients for TM_0, TM_2, TM_4, …, TM_{20} modes are obtained as the ratio of the transmitted and the incident modes as shown in Fig. 4(a). The same

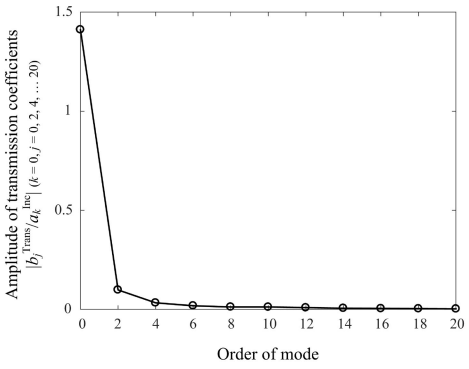

(a) Transmission coefficients at Junction 1

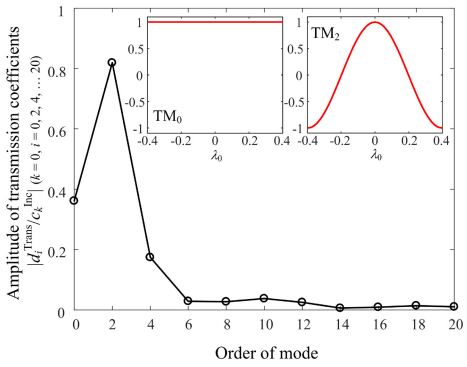

(b) Transmission coefficients at Junction 2

Fig. 4. Amplitude of transmission coefficients at Junctions 1 and 2.

DOI: 10.1587/elex.15.20180612
Received June 12, 2018
Accepted June 19, 2018
Publicized July 2, 2018
Copyedited July 25, 2018

condition is applied to Junction 2 as shown in Fig. 3(b) and the amplitudes of transmission coefficients are presented in Fig. 4(b).

The subscript numbers in TM indicate the number of zero crossings in the H_y-field [6]. As can be seen in the Fig. 4(a), the amplitude of TM_0 predominates over the amplitudes of other modes because the higher order modes less contribute to the satisfaction of boundary conditions at Junction 1. On the other hand, at Junction 2, the amplitude of TM_2 is greater than TM_0 as shown in Fig. 4(b). By using not only the transmission coefficients but also reflection coefficients, the overall transmittance of Fig. 1 can be obtained as a function of plate thickness w using the multilayer problems [13].

4 Transmittance and discussion

Fig. 5 presents the transmittances of PEC and Al plates at three frequencies of 30, 50, and 200 THz with $p = 0.8\lambda_0$ and $2h_v = 0.05\lambda_0$. In the case of PEC, the peak values of 1 imply 100% transmission when the thickness w is $0.405\lambda_0$. The peaks are repeatedly observed with interval of half wavelength $(0.405 + 0.5n)\lambda_0$, where n is integer, which is well known as the Fabry-Pérot resonance (FPR). For Al at 30 THz, on the other hand, the maximum peak of 0.61 is observed when w is $0.388\lambda_0$, and the peak is less than that of PEC due to the loss of the real metal. The numbers of modes in MIM slit and free space are $N_M = 70$ (point spectrum = 20, DCS = 50) and $N_F = 21$, respectively.

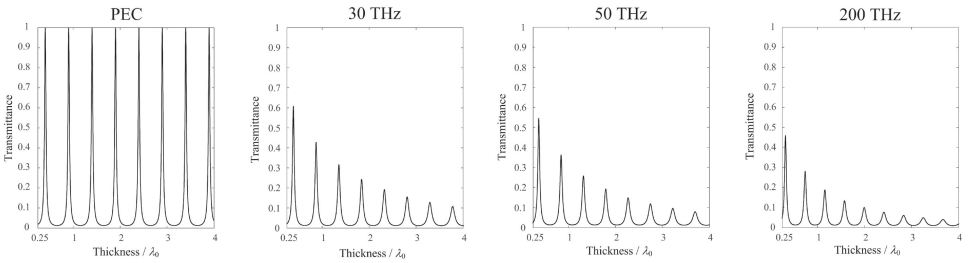

Fig. 5. Transmittance versus plate thickness w ($2h_v = 0.05\lambda_0$, $N_M = 70$, and $N_F = 21$).

The FPR is also found; however, the peaks are attenuated as the thickness w of the plate increases. The maximum peaks from 30 THz to 200 THz are gradually decreased from 0.61 to 0.46, and this attenuation can be explained by the NPC in Table III. The $|\mathrm{Im}(k_{z,n}/k_0)|$ in the NPC changes from 0.929×10^{-2} to 1.814×10^{-2} as frequency increases from 30 THz to 200 THz. In addition, the intervals of the peaks are shortened as the frequency increases because $\mathrm{Re}(k_{z,n}/k_0)$ goes from 1.035 to 1.197. The transmittances with the changed gap width as $2h_v = 0.1\lambda_0$ are shown in Fig. 6. Repeated peaks are similarly observed for PEC and Al plates.

Fig. 7 presents transmittance comparisons between the Al and Ag plates when the gap width ($2h_v$) is changed as $0.2\lambda_0$ while other conditions are the same. The overall transmittances increase compared to those in Figs. 5 and 6 due to the wider gap width. The transmittance patterns for both metals are almost overlapped at 30 and 50 THz, however, the patterns at 200 THz show a slight difference. The transmittances of Al (maximum of 0.83) are slightly greater than those of Ag

DOI: 10.1587/elex.15.20180612
Received June 12, 2018
Accepted June 19, 2018
Publicized July 2, 2018
Copyedited July 25, 2018

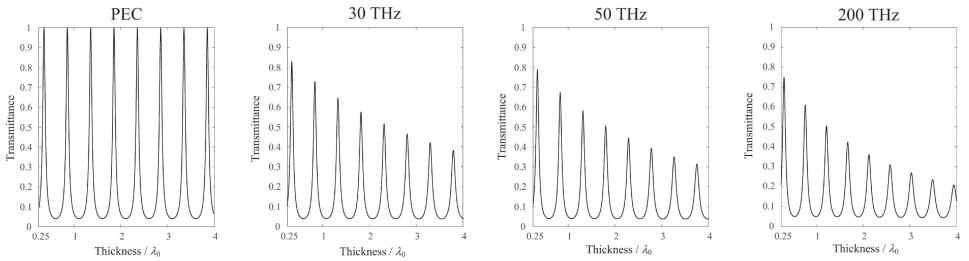

Fig. 6. Transmittance versus plate thickness w ($2h_v = 0.1\lambda_0$, $N_M = 70$, and $N_F = 21$).

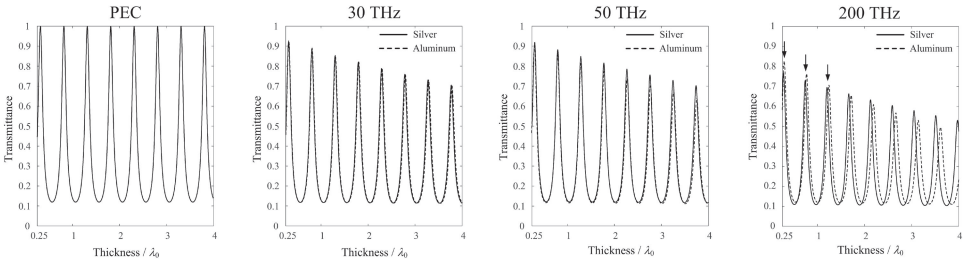

Fig. 7. Transmittance versus plate thickness w ($2h_v = 0.2\lambda_0$, $N_M = 70$, and $N_F = 21$).

(maximum of 0.77) up to first three peaks as indicated by arrows. However, the transmittances of Al decrease rapidly than Ag as the plate thickness increases over about $2\lambda_0$. Interesting phenomena are also observed in which different intervals of the transmission peaks are found between Al and Ag.

The normalized propagation constants for the first and the second modes from Table III can be applied into the wave propagation terms. The $|\exp(-jk_{(z,0)}w)|$ and $|\exp(-jk_{(z,2)}w)|$ are approximately 0.995 and 4.76×10^{-4}, respectively, when $2h_v = 0.2\lambda_0$, $w = 0.25\lambda_0$, and metal is Ag at 200 THz. From the magnitudes, the propagating mode ($n = 0$) has dominant effect on the transmission while the magnitude of the first evanescent mode ($n = 2$) is small compared with the propagating mode and little affects. Also, the magnitudes by higher order modes ($n = 4, 6, 8, \ldots$) are much smaller and little contribute to the transmission, however, they are important to correctly enforce the boundary conditions.

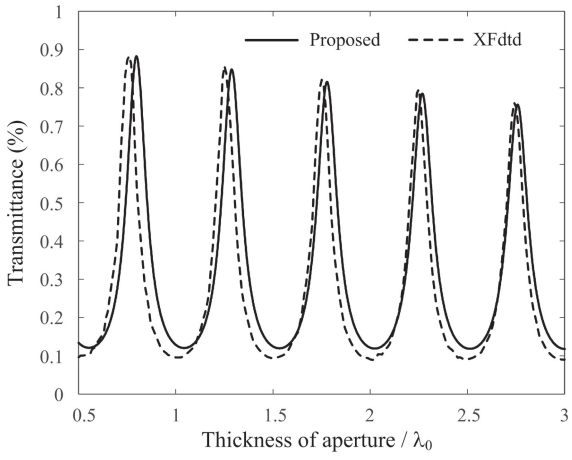

Fig. 8. Comparison of the transmittance properties ($2h_v = 0.2\lambda_0$, $N_M = 70$, and $N_F = 21$).

DOI: 10.1587/elex.15.20180612
Received June 12, 2018
Accepted June 19, 2018
Publicized July 2, 2018
Copyedited July 25, 2018

Fig. 8 presents the comparison of the transmittances between proposed results and simulation results calculated by 3-D EM simulation software (XFdtd) from REMCOM [15]. To compare the transmittance characteristics under the same condition, the type of metal is silver (Ag) and frequency is fixed at 50 THz with $p = 0.8\lambda_0$, $2h_v = 0.2\lambda_0$. The same numbers of modes ($N_M = 70$ and $N_F = 21$) are used in MMT. The maximum transmittance of the proposed result is 0.87, which is similar to the simulated value of 0.88, and the entire transmittance trends are similar to each other. Slight discrepancy in transmittances are observed between the XFdtd and the MMT due to the different numerical techniques. The results from the XFdtd are obtained by the FDTD numerical method, and we applied the Debye-Drude model to approximate the relative permittivities of the real metal. Despite the subtle difference, the overall trends are similar to each other.

Fig. 9(a) shows the magnetic field distributions for the PEC periodic slit at the plate thicknesses (w) of $1.32\lambda_0$ and $1.07\lambda_0$, which are the plate thicknesses for the maximum and minimum transmittances. At resonance with $w = 1.32\lambda_0$, the strong magnetic field intensity is exhibited in the gap of Region 2, while the weak field intensity is observed in Region 1. At off-resonance with $w = 1.07\lambda_0$, the repetitive strong field intensity is observed in Region 1, which results in a high standing wave ratio. Similar to the PEC case, the resonant transmission phenomena for the real metal of Al can be explained as shown in Fig. 9(b). Another noteworthy observation of Al is that the field intensity can now be found in the metal region of the MIM near the boundary between the insulator and the metal. This proves that the real metal at the higher THz frequency behaves differently compared to the PEC.

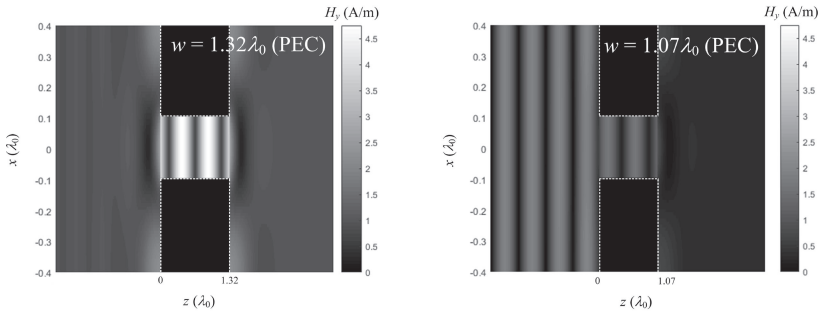

(a) PEC ($w = 1.32\lambda_0$, and $1.07\lambda_0$)

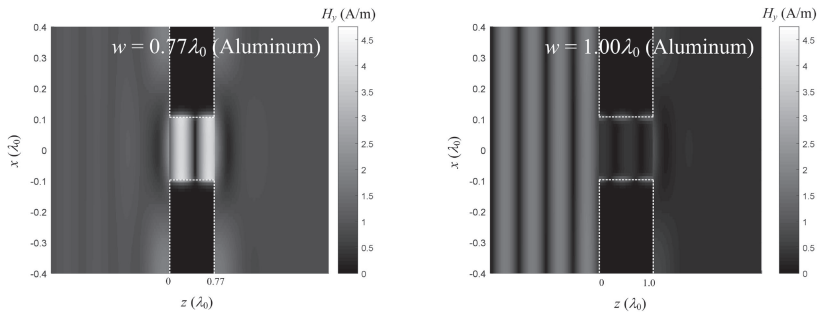

(b) Al ($w = 0.77\lambda_0$, and $1.00\lambda_0$)

Fig. 9. Contour plots of the magnetic field intensities.

DOI: 10.1587/elex.15.20180612
Received June 12, 2018
Accepted June 19, 2018
Publicized July 2, 2018
Copyedited July 25, 2018

Table III. Normalized propagation constants ($k_{z,n}/k_0$) in the periodic MIM slit

Gap width $2h_v$	Propagating mode ($n = 0$)	1st Evanescent mode ($n = 2$)
$0.05\lambda_0$ PEC	1	$-j19.98$
$0.05\lambda_0$ Al (30 THz)	$1.035 - j9.292 \times 10^{-3}$	$8.895 \times 10^{-4} - j19.97$
$0.05\lambda_0$ Al (50 THz)	$1.055 - j1.183 \times 10^{-2}$	$1.007 \times 10^{-3} - j19.97$
$0.05\lambda_0$ Al (200 THz)	$1.197 - j1.814 \times 10^{-2}$	$-1.192 \times 10^{-2} - j19.97$
$0.1\lambda_0$ PEC	1	$-j9.950$
$0.1\lambda_0$ Al (30 THz)	$1.018 - j4.732 \times 10^{-3}$	$9.484 \times 10^{-4} - j9.946$
$0.1\lambda_0$ Al (50 THz)	$1.028 - j6.079 \times 10^{-3}$	$1.195 \times 10^{-3} - j9.944$
$0.1\lambda_0$ Al (200 THz)	$1.103 - j9.891 \times 10^{-3}$	$3.236 \times 10^{-4} - j9.934$
$0.2\lambda_0$ PEC	1	$-j4.899$
$0.2\lambda_0$ Al (30 THz)	$1.008 - j2.392 \times 10^{-3}$	$9.777 \times 10^{-4} - j4.895$
$0.2\lambda_0$ Al (50 THz)	$1.014 - j3.092 \times 10^{-3}$	$1.259 \times 10^{-3} - j4.893$
$0.2\lambda_0$ Al (200 THz)	$1.053 - j5.249 \times 10^{-3}$	$1.824 \times 10^{-3} - j4.878$
$0.2\lambda_0$ Ag (30 THz)	$1.012 - j2.348 \times 10^{-3}$	$9.576 \times 10^{-4} - j4.894$
$0.2\lambda_0$ Ag (50 THz)	$1.020 - j2.401 \times 10^{-3}$	$9.684 \times 10^{-4} - j4.891$
$0.2\lambda_0$ Ag (200 THz)	$1.081 - j3.235 \times 10^{-3}$	$7.831 \times 10^{-4} - j4.870$

5 Conclusion

We have investigated the resonant transmission through a periodic MIM slit on real metal of Al and Ag plates in the THz range. The transmittance properties of the real metal were compared with those of PEC as functions of the frequency, the gap width, and the thickness of the MIM plate. In the case of PEC, the peak transmittance of 1 was repeatedly observed at half wavelength intervals $(0.405 + 0.5n)\lambda_0$. On the other hand, a lower peak transmittance of 0.61 for the real metal (Al) was observed when $w = 0.388\lambda_0$ at 30 THz. The intervals and attenuations of the resonant transmission peaks were closely related to the NPCs of the propagating mode. The resulting transmittance (0.87 when $p = 0.8\lambda_0$, $2h_v = 0.2\lambda_0$, and Ag) was then verified against the simulated value (0.88 at the same conditions) obtained from a commercial EM simulator. Finally, the magnetic field distributions at resonance and off-resonance for PEC and real metal (Al) were observed near the periodic slits. This study demonstrated that the proposed MMT is suitable for calculating the transmittance of the periodic MIM slits on the real metal material and provided in-depth intuition for resonance phenomena using the modal approach.

Acknowledgments

This research was partly supported by ICT R&D program of MSIP/IITP 2016-0-00130, Basic Science Research Program through the National Research Foundation of Korea (NRF) funded by the Ministry of Education (No. 2015R1A6A1A03031833), and the Korea Institute of Nuclear Safety under the project "Development of Proof Test Model and Safety Evaluation Techniques for the Regulation of Digital I&C Systems used in NPPs" (No. 1805006-0118-SB110).

DOI: 10.1587/elex.15.20180612
Received June 12, 2018
Accepted June 19, 2018
Publicized July 2, 2018
Copyedited July 25, 2018